Detection of NH$_3$ gas using CrVO$_4$ nanoparticles

David John Dmonte [a], Aman Bhardwaj [b], Pelin Kavraz [c], Rostislav Slobodian [a], Jan Antos [a], Orhan Sisman [d], Dusan Galusek [d,e], Thomas Fischer [b], Sanjay Mathur [b,*], Ivo Kuritka [a,f,**]

[a] Centre of Polymer Systems, Tomas Bata University in Zlín, Tr. Tomase Bati 5678, 760 01 Zlín, Czech Republic
[b] Institute of Inorganic Chemistry, University of Cologne, Greinstr. 6, 50939 Cologne, Germany
[c] Department of Physics, Faculty of Science, Istanbul University, 34314 Vezneciler, Istanbul, Turkey
[d] Centre for Functional and Surface Functionalized Glass, Alexander Dubček University of Trenčín, Študentská 2, 91150 Trenčín, Slovakia
[e] Joint Glass Centre of the IIC SAS, TnU AD, and FChPT STU, 91150 Trenčín, Slovakia
[f] Department of Chemistry, Faculty of Technology, Tomas Bata University in Zlín, Vavreckova 5669, 760 01 Zlín, Czech Republic

ARTICLE INFO

ABSTRACT

Nanostructured chromium orthovanadate with an average particle size of 65 nm was prepared by the co-precipitation technique for the chemiresistive sensor. The morphology and particle size distribution of CrVO$_4$ nanoparticles were examined by SEM and TEM. According to XRD, most of the prepared CrVO$_4$ material (crystallites) has a monoclinic structure belonging to the space group C2/m. XPS and UV-Vis absorbance measurements provided additional information on the main phase and the surface. The material has shown reasonable selectivity towards the NH$_3$ gas. The as-prepared CrVO$_4$ nanostructures exhibit a maximum relative response of 32% to 50 ppm NH$_3$. The identical dynamic response profiles during the sequential injections of 50 ppm NH$_3$ evinced the repeatability of the sensor. The limit of detection (LOD) value of the sensor was estimated ca 0.7 ppm using relative response values towards a wide range of NH$_3$ concentrations from 10 ppm to 100 ppm. The sensing mechanism was expressed in terms of the surface band bending phenomenon caused by the adsorption and desorption of the ammonia. The best sensor performance was achieved at 330 °C, where the effects of humidity and moisture can be neglected. The results confirmed that the CrVO$_4$ nanomaterial has the potential to fabricate an affordable, easy-to-make, and reliable gas sensor for NH$_3$ gas.

1. Introduction

New gas sensors have been developed and used in a number of sectors in the last few decades for the applications including environmental monitoring, automotive industry, medical applications, and indoor air quality control [1–4]. Precautionary monitoring of gases like CO, CO$_2$, NO, N$_2$O, NO$_2$, SO$_2$, SO$_3$, NH$_3$, and etc. is important for a sustainable future as concerns about climate change and public health grow. Ammonia is one of the harmful gases used in a variety of industries [5–11]. The agricultural industry, and specifically the animal husbandry, is where the majority of NH$_3$ that enters our environment is released [12]. Since ammonia is very reactive in gaseous form, its lifespan might range from a few hours to days [13,14]. Despite its widespread presence, ammonia is not typically considered a significant health hazard at usual levels. However, when ammonia reacts with other atmospheric chemicals, such as sulfuric and nitric acid, it can contribute

to the formation of secondary inorganic particles, significantly impacting human health [15,16]. Chronic exposure to these particles in urban areas has been associated with 307,000 premature deaths in the 27 EU Member States in 2019 [17]. In addition to its indirect impact on human health, ammonia can also adversely affect the environment. It can contribute to the acidification of natural habitats, harming aquatic organisms and affecting the delicate balance of these ecosystems [18]. It is well known that excessive NH$_3$ concentrations directly cause chronic and acute damage (such as slowed growth and grayed-white foliage) to plants and can directly affect food security [19]. Despite its potential impact, ammonia levels in ambient air are currently not regulated in Europe, as there are no official limit values or threshold values. Ammonia also has medical applications, as it is considered a useful biomarker for medical diagnostics [20]. By analyzing exhaled breath, healthcare professionals can detect elevated levels of ammonia, which can indicate kidney failure [21]. The correlation between ammonia

Table 1
Comparative sensing studies towards to detect NH_3.

Sample	LOD	Usage of Noble metals	Operating Temperature	Material feature size
ZnO[28]	50 ppm	no	150 °C	20 - 30 nm nanoparticles
ZnO/SnO2[29]	46 ppm	no	100 °C	15 / 20 nm nanoparticles
Pd-Co@IRMOF-1[31]	1 ppm	yes	Room Temperature	5 - 10 nm nanoparticles
ZIF-67/rGO[32]	20 ppm	no	Room Temperature	530 ± 50 nm nanoparticles
MAPbBr$_{3-x}$I$_x$ [33]	50 ppm	no	15 °C	Thin film
Mesoporous Pt-WO$_3$[44]	200 ppm	yes	125 °C	9-10 nm pore size
CrVO$_4$ (this work)	10 ppm	no	330 °C	60-70 nm nanoparticles

concentrations in breath and blood urea nitrogen makes the use of chemiresistive gas sensors for breath analysis a practical and straightforward approach to medical diagnostics [22–24]. Consequently, regulating ambient air and specific ammonia concentrations is essential.

There exists a broad range of various sensor types, including surface acoustic wave sensors, optical gas analyzers, amperometric gas sensors, potentiometric gas sensors, and catalytic field effect devices. [25]. The simplicity and performance of chemiresistive gas sensors make them suitable in most case scenarios for detecting ammonia [26]. As part of the Internet of Things (IoT) revolution, the innovation requirement for the construction of intelligent sensors of NH_3 could be used in conjunction with complementary metal oxide semiconductor (CMOS) circuits [27].

Materials such as standard monometallic oxides such as ZnO in thin film chemiresistive sensing show a detection level of 50 ppm at 150 °C [28]. In another approach Ishpal et al. used ZnO nanoparticles to sense up to 46 ppm of NH_3 at 100 °C [29]. Bimetallic oxides have also been extensively used in innovative sensing methods [30]. Khan et al. have presented an interesting use of a bimetallic alloy loaded in MOF with a limit of detection up to 1 ppm of NH_3 at room temperature, although with the usage of noble elements such as Pd, making it non-viable for practical use in consumer electronics [31]. Another interesting composite material using zeolites and reduced graphene oxide employs a complicated material preparation process. It has been shown to detect 20 ppm of NH_3 at room temperature. [32]. Perovskite structures in doped and undoped forms are also used as active materials for sensing ammonia. They have been modified structurally to show better properties in applications for gas analyte detection. [33].

Similarly, there has recently been renewed interest in AVO_4 structures for applications in oxygen evolution reaction, super protonic conductors, high-performance cathode material and photocatalytic research [34–37]. These oxides have been the subject of several studies due to their unique properties, such as ionic conductivity [38]. The isostructural polymorphs, such as $FeVO_4$ nanorods, have recently been proposed to detect volatile organic compounds [39]. Several vanadium-based bimetallic oxides, including rare earth and transition metal vanadates such as $CeVO_4$, $BiVO_4$, and $InVO_4$, have been developed to detect NH_3, showing good performance [40–42]. Among them, $CrVO_4$ has recently been used to detect NH_3 as a high-temperature potentiometric sensor that shows exquisite selectivity, albeit at a high operating temperature [43]. .

In the present work, we investigate the chemiresistive NH_3 gas sensing properties of $CrVO_4$ for the first time. The sensor fabrication and optimal operating temperature were analyzed. The NH_3 response and recovery rate, repeatability, and relative response (relative change of the original resistance of the sensor, expressed in %) LOD (Limit of detection) were also studied. According to the experimental findings, $CrVO_4$

has a significant potential as an ammonia-detecting active material for chemiresistive gas sensing.

2. Experimental

2.1. Materials and sample preparation

A modification of the co-precipitation process described by Lan et al. [45] was used to synthesise $CrVO_4$. 1 mM chromium nitrate was dissolved in 50 mL of deionized (DI) water. Similarly, 50 mL of warm DI water was used to dissolve 1 mM of ammonium metavanadate. The solutions were then mixed and stirred for an additional two hours. After that, a precipitate was formed and carefully collected. The precipitate was then rinsed three times with ethanol and DI water. Then it was calcined in a tube furnace for two hours at 600 °C in an argon atmosphere, yielding the desired product, $CrVO_4$.

The powder sample was dissolved in α-terpinol, 10% by weight. 10 μL of the solution was added onto a 4-pin-TO39 prepared sensor substrate from UST Umwelt sensor Technik GmbH. The sensor was dried for 18 h at 80 °C to ensure its long-term stability and a smooth surface. The sensor was then heated at 500 °C for two hours to prepare it for testing and gas sensing measurements. Three sensor specimens were prepared using the same methodology.

2.2. Characterization techniques and methodology

The surface morphology and particle shape were examined using a field emission scanning electron microscope (FE-SEM), and elemental analysis was performed using an energy dispersive X-ray spectroscopy (EDX) assembled in Nova NanoSEM450 scanning electron microscope setup (FEI, United States). Transmission electron microscopy (TEM) of the material was performed using a JEOL TEM microscope JEM – 2100/HR (Japan). The MiniFlex 600 XRD diffractometer (RIGAKU, Japan) was employed to conduct X-ray diffraction measurements utilizing Co Kα radiation (λ = 0.179 nm). The voltage and emission current were set at 40 kV and 15 mA, respectively. The diffraction patterns were recorded in the range of the diffraction angles 2θ from 3° to 90° at a scanning speed of 6° min^{-1}. An external NIST® SRM® 660c line position and line shape standard LaB_6 purchased from Merck (MERCK spol. s r. o., Prague, Czechia) was used for coherently diffracting domain average size estimation with the aid of Halder-Wagner method.

FTIR spectra were collected in ATR mode with diamond crystal using a Nicolet iS5 spectrometer (Thermo Fisher Scientific, USA). The spectral resolution was 4 cm^{-1}, and the number of scans was 64. The Raman spectra of the sample were acquired using a Nicolet DXR Raman microscope (Thermo Scientific, USA) with an Olympus optical microscope equipped with an objective with the 50X magnification. A laser (532 nm) was used as the excitation source. A high-resolution grating of 1800 lines per millimeter was installed, providing a spectral resolution of 0.9642 cm^{-1}. Spectra were collected with 5 s exposure and 20 scans. UV visible spectra were acquired using UV–vis spectrophotometer SPE-CORD 210 Plus (Analytik Jena AG, Germany) for the optical study of the freshly synthesized sample. The spectra show a wavelength ranging from 200 to 800 nm in diffuse reflectance mode. XPS analysis was performed using a Thermo Scientific Nexsa G2 instrument (ThermoFisher Scientific Co., Waltham, MA, USA), employing an Al Kα X-ray source with a spot size of 400 μm. The analyzer's pass energy was adjusted to 100 eV with a 1.0 eV energy step size for obtaining general spectra of $CrVO_4$ powder. For elemental spectra, the pass energy was set to 50 eV with a 0.1 eV step size. The Avantage v.5 software (ThermoFisher Scientific Co., Waltham, MA, USA) was used for data acquisition and processing. Using the ASAP® 2020 Plus: Accelerated Surface Area and Porosimetry System (Micromeritics Instrument Corp., USA) the pore characteristics and surface area of the sample were studied and analyzed using the Brunauer-Emmett-Teller (BET) technique.

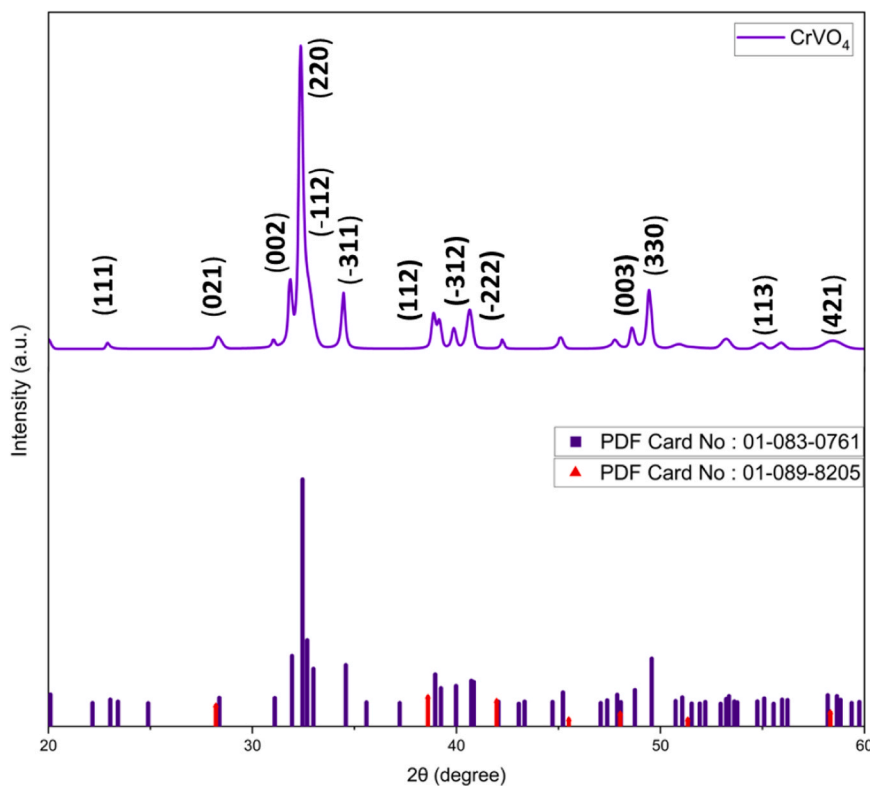In an arrangement shown in the supplementary material in Fig. S1,

Fig. 1. XRD patterns of synthesized CrVO₄ sensing material and the corresponding PDF card data.

gas sensing measurements were examined in a 250 mL airtight container with gas injection and exhaust provision. The required concentration (ppm) was reached by mixing the analyte gas flow with the synthetic air gas flow while utilizing two mass flow controllers (Aera FC-7700 C). The background environment was generated using a dry air gas cylinder (Air Products and Chemicals, Inc., certified for 0% humidity) to rule out surface moisture interactions. The target gases (NH_3, CO, NO_2, and C_2H_6O) in certified gas cylinders were diluted for the measurements. Using a Keithley K2700 (Solon, Ohio, USA) data acquisition system, the resistance to exposure to air and analyte mixtures was constantly monitored from the sensor. For precise heating, a calibration curve was created between voltage and temperature. The platinum heater on the sensor substrate TO-39 was powered by the Elektro Automatik power source meter, model ES-PS 3065–03B.

A specially developed LabVIEW application was used to run and operate every system and component in this arrangement and collect experimental data. The sensor responds to the change in ammonia concentration in the measurement chamber by changing its electrical resistance *R,* which is recorded. Moreover, the following formula was used to calculate the relative response expressed in per cents, $100 \cdot \Delta R / Ra$, to the presence of the target gas analyte.

$$Relative \quad Response(\%) = 100 \bullet \Delta R \Big/ Ra = \frac{Ra - Rg}{Ra} \bullet 100 \qquad (1)$$

$$Relative \quad Response(\%) = 100 \bullet \Delta R \Big/ Ra = \frac{Rg - Ra}{Ra} \bullet 100 \qquad (2)$$

For reducing gases, Eq. (1) was applied while for oxidizing gases, Eq. (2) was emplyed. The symbols *Rg* and *Ra* represent the resistance values of the sensors in the presence of target gas and synthetic air, respectively. Their difference ΔR is calculated according to the character of the gas. The acronyms T-90 response and T-90 recovery time refer to the time required for the sensor to saturate to 90% of total resistance [46, 47]. Gas sensing measurements were performed once a stable baseline had been achieved, after a preconditioning time of 2 h at optimal

temperature.

3. Results and discussions

3.1. Material characterization

The data in Fig. 1 represent the X-ray diffraction patterns of the CrVO₄ material. The powder was identified as the monoclinic phase of the CrVO₄ based on agreement with the PDF Card No: 01–083-0761. The (001), (110), (021), (220), (−112), (−311), (−222), (400), (003), (−223), (113), (−511) and (421) crystallographic planes were indexed to the XRD diffraction maxima at 2θ values of 15.81°, 16.07°, 28.38°, 32.46°, 32.69°, 34.58°, 40.85°, 45.22°, 48.75°, 53.22°,55.09°, 55.96° and 58.65°, respectively. This indicates that the synthesised substance belongs to the orthovanadate family with the general formula MVO₄. The database also identifies a very small quantity of chromium-vanadium oxide ($Cr_xV_{1-x})_2O_3$ in the trigonal crystal system belonging to the R-3c space group, as some diffraction lines overlap and match PDF Card No: 01–089-8205. This could be attributed to a minor quantity of unspent precursor or a possible formation of a byproduct as the impurity in CrVO₄ [48]. However, most of the diffraction pattern matches the crystal structure of CrVO₄-I [43].

The structure in polyhedral form is shown in the supplementary document in Fig. S2. The CrVO₄-I phase belongs to the monoclinic C2/m space group. The key feature is the presence of two different forms of CrO₆ octahedra and VO₄ tetrahedra unlike one form in the orthorhombic (CrVO₄-III) phase. As reported by Tetsuya et al., the crystal structure is influenced by calcination temperature[49]. They have shown that CrVO₄-I activity for selective oxidation requires optimisation of the calcination temperature and that the bridging oxygen in V-O-Cr bonds is the structural moiety responsible for the catalytic activity favouring thus the monoclinic phase over orthorhombic phase of CrVO₄ for such purpose. Using external standard LaB₆ and Halder-Wagner method, the average size of coherently diffracting domains is (42.1 ± 0.5) nm suggesting preparation of ca two times larger crystalline nanodomains than
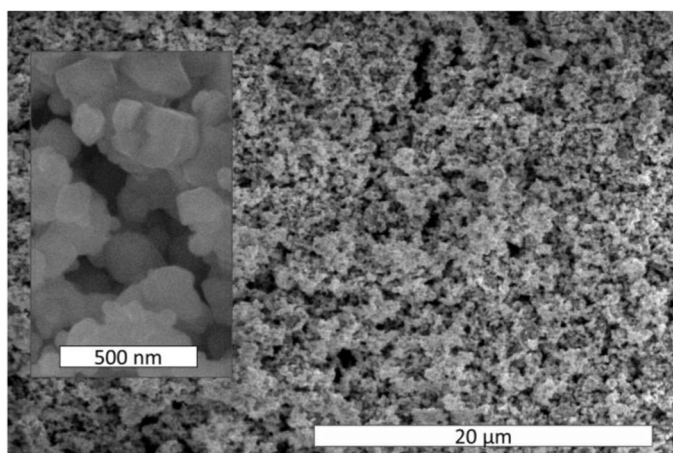
Fig. 2. SEM image of synthesized chromium vanadate (inset shows a detail at higher magnification) showing that the larger particles consist of smaller nanoparticles.

in synthesis published by other authors who used sucrose carbonization supported preparation technique[36].

In Fig. 2, the SEM micrograph shows the morphology of $CrVO_4$ particles. The nanoparticles are aggregated and agglomerated, and randomly distributed, making the surface of the material rough. They are about 100 nm in size and have an irregular shape, indicating polycrystallinity. This is in agreement with the estimation of the average size of coherently diffracting domains obtained from XRD analysis. Such morphology can potentially aid the gas sensing ability because of the increased surface area. Such structure may also affect the electrical conduction mechanism, as shown by Shreenivasa et al. [36].

Energy-dispersive X-ray spectroscopy (EDS) was performed to reveal elemental composition of the material. A 12 micrometers long line scan was performed at the prepared sample surface, and the recorded SEM image and the compositional graph are shown in the supplementary file in Fig. S3 and Fig. S4. In spite of local variations and noise, the ratio between Cr and V atoms continues to be almost perfect (1:1) showing an average value of 1.00 ± 0.08 ($\pm$ indicating standard deviation). The intercept value of a constant linear fit (with slope fixed at 0) is 1.002 ± 0.008 ($\pm$ indicating standard error), see the Supplementary file Fig. S5. The analysis confirms the presence of the target elements Cr, V,

and O, as reported in similar research by Yogeeshwari et al. [50]. The average atomic concentration of Cr was (18 ± 3) %, V was (18 ± 3) %, and O was found (64 ± 6) % suggesting almost ideal stoichiometric ratio 1:1:3.6 corresponding to a formula $CrVO_{3.6}$ which agrees to $CrVO_4$ formula within the experimental error.

As shown in Fig. 3, a representative TEM image (A) shows that the oblong-shaped agglomerate/aggregate particles are composed of nanoparticles with the size well below 100 nm. A high fraction of the particles between 50 nm and 70 nm is manifested in the inset showing the particle size distribution. However, there appears to be a wide distribution between 20 and 100 nm in general, which is consistent with expectations based on the literature [37]. In the second image (B), we calculate the *d* spacing in the images after the required processing to obtain a fringe distance profile and the average calculated d spacing of 0.32 nm and 0.31 nm, as shown in the Supplementary File Fig. S6 and S7. This seems to match, with high accuracy, the hkℓ lattice planes with Miller indices of (220) and (−112) corresponding to X-ray diffraction maxima at 2θ = 32.46° and 32.69° (PDF Card No.: 01-083-0761).

The liquid N_2 adsorption analysis resolved the pore characteristics and the specific surface area of the sample using the Brunauer-Emmett-Teller (BET) technique. Fig. S8 shows the adsorption isotherm, and Fig. S9 shows the BET analysis results. The physisorption isotherms belong more to type-III, which typically is the result of a weak interaction between the sample surface and the adsorbate. It signifies that multiple layers of gas adsorbate are quickly formed, pointing towards a nonporous surface, which showed a calculated mean pore diameter of 29.2 nm, which is comparable to the size range of irregularly shaped particles observed by electron microscopy. The specific surface area was $8.3 \ m^2 \ g^{-1}$, which corresponds to the data reported in other works, partly due to high-temperature synthesis [51].

The fingerprint region of the FT-IR spectrum of $CrVO_4$ nanoparticles is shown in Fig. 4(a). The main vibrational bands, assigned to mixed bridging of the V – O – V and Cr – O – V stretching, are found in the wavenumber range of 1000 cm^{-1} to 550 cm^{-1}. The IR bands between 1050 cm^{-1} and 880 cm^{-1} can be assigned to the terminal V – O stretching according to reports on isostructural polymorphs by Yusuf et al. [52]. The band at 721 cm^{-1} represents mixed bridging stretching of V – O – Cr, while the bands at 862 cm^{-1} and 923 cm^{-1} can be attributed to V – O asymmetric and symmetric stretching vibrations, respectively [53,54]. The bands between 410 cm^{-1} and 424 cm^{-1} correspond to Cr – O stretching vibrations in $CrVO_4$ [55,56]. Essential deformation vibrations of the V – O – V bridges can be observed at
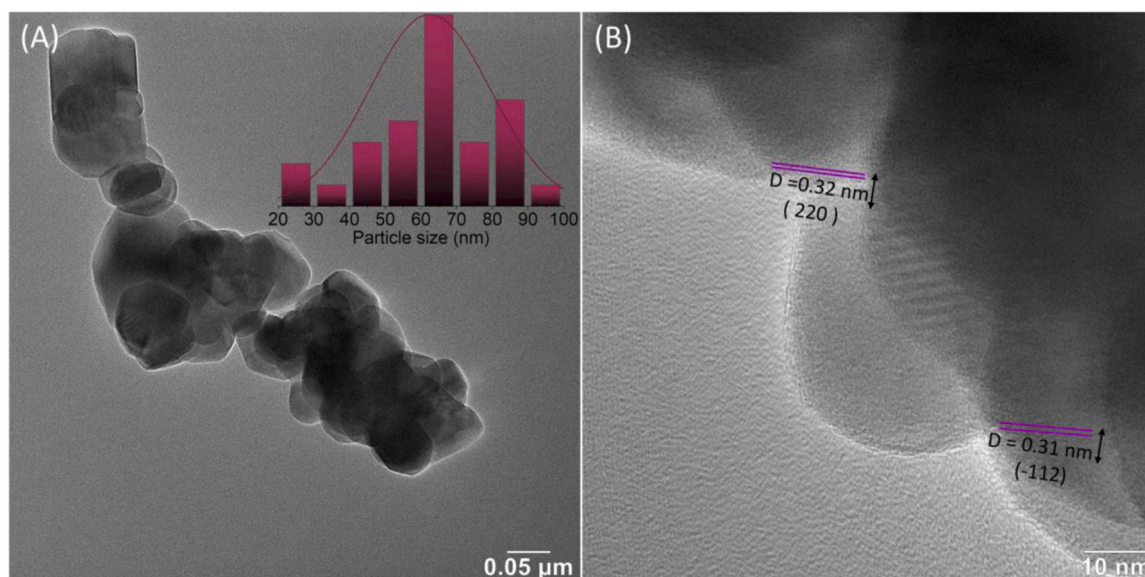

Fig. 3. TEM image of synthesized a) Chromium vanadate material with the particle size distribution b) Lattice fringes calculated to match the hkℓ lattice planes.
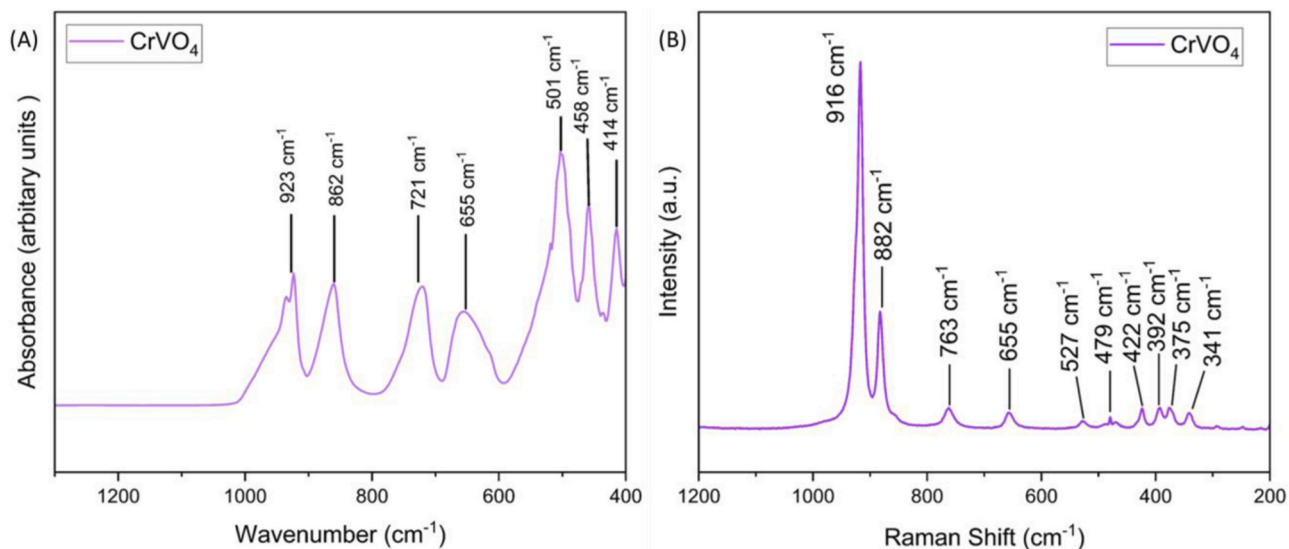
Fig. 4. The FT-IR spectra a), and Raman spectra b) of synthesized $CrVO_4$ sensing material.
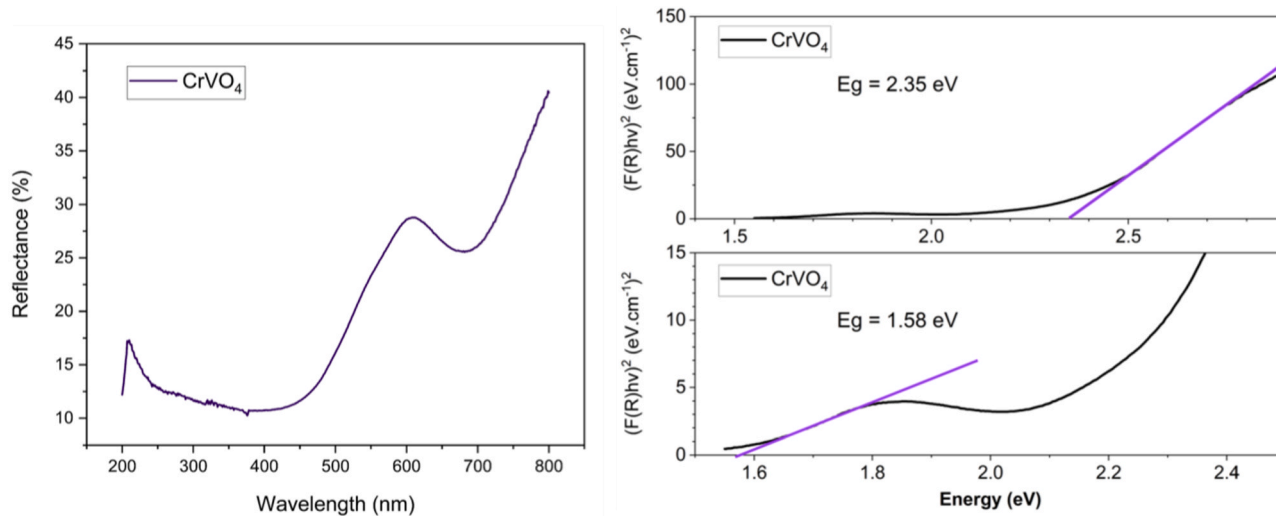

Fig. 5. Left panel: A) Reflectance spectra of the synthesized $CrVO_4$ sensing material; right panel: Tauc plot using the transformation of the reflectance to the Kubelka-Munk function to find the intercepts according to [65]. The upper graph B) finds the band gap for the $CrVO_4$ typical absorption, whereas the lower graph C) evaluates the optical transition associated with the low energy shoulder peak at ca 700 nm.

450 cm^{-1} and 501 cm^{-1}, as reported previously [53,57].

The Raman spectrum of the material is shown in Fig. 4(b). An interpretational analogy can be found in the spectra of $FeVO_4$, which is a close polymorph. Bera et al. explain that the emergence of all bands at higher wave numbers from 580 cm^{-1} to 1000 cm^{-1} signifies the V-O-Fe and V=O stretching, whereas the lower frequency modes are similarly noted intensity peaks for relative torsional motion between polyhedrons [58,59]. The most notable modes between (915 cm^{-1} – 930 cm^{-1}) are assigned to the symmetric bending and asymmetric stretching of the V-O bonds. The shoulder peak at 882 cm^{-1} is attributed to the presence of a precursor impurity or byproduct. The modes between 270 cm^{-1} and 380 cm^{-1} are known to correspond to pure rotation and symmetric bending of tetrahedral VO_4 units [60–62]. Additionally, the modes between 380 cm^{-1} and 502 cm^{-1} are related to symmetric bending and asymmetric bending of tetrahedral VO_4 units. The other consistent bands are at 527 cm^{-1}, 655 cm^{-1} and 763 cm^{-1}. The former is assigned to the mixed stretching of V – O – Cr bridging, while the latter two can be associated with the symmetric and two asymmetric stretching modes of isolated VO_4 tetrahedra as found in other orthovandates such as $CeVO_4$

and $NdVO_4$ [63,64] These vibrational studies confirmed the presence of the bonds allowing for a more cleaved and well-distributed unit cell lattice, which might be beneficial for future gas sensing applications.

The optical properties of the synthesised $CrVO_4$ were investigated, and the resulting absorbance spectra are shown in Fig. 5(a). The reflectance of $CrVO_4$ does not increase beyond 15% due to relativeky high absorption in the wavelength range between 200 nm and 500 nm. Between 500 nm to 800 nm, the reflectance increases quickly to 30%, albeit a small deviation from the trend forms a shoulder peak at 700 nm, after which the reflectance rises to 40% at 800 nm. This means less energy is absorbed in the near-infrared region. It is well known that the optical band gap and light absorption are related to the positions of the energy band of the semiconductor [65,66], as expressed by Eq. 3.

$$[\alpha h\nu]^{1/\lambda} = B(h\nu - E_g) \tag{3}$$

Where B is a constant, h is the Planck constant, ν is the photon frequency, α stands for the optical absorption coefficient, E_g is the band gap energy, and λ factor represents the nature of the electronic transition and is equal to 1/2 for direct transition and 2 for indirect transition. As
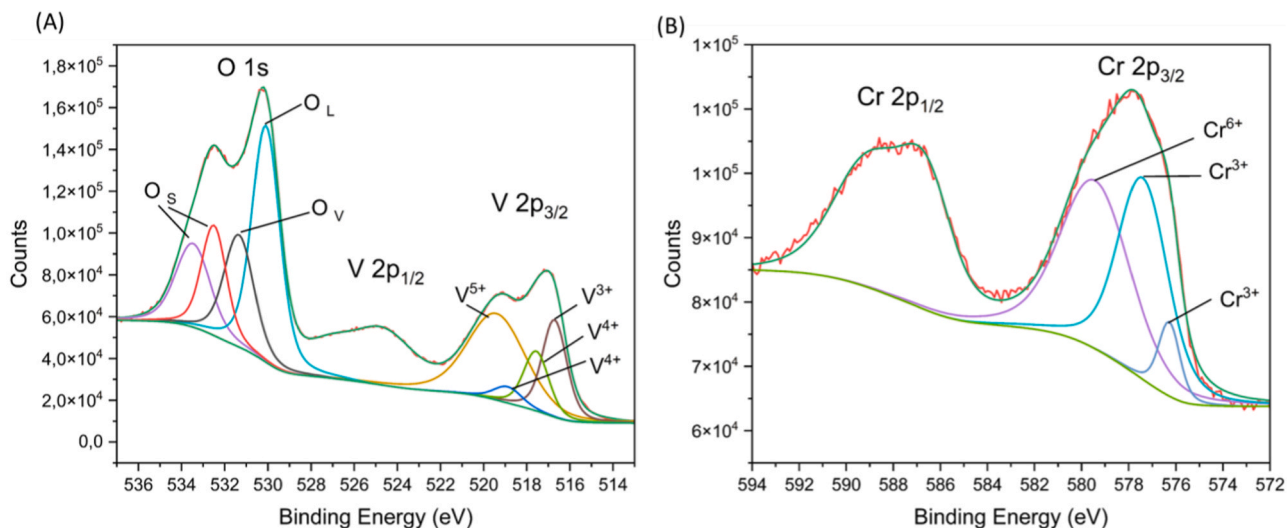
Fig. 6. High-resolution photoelectron spectra of a) V 2p and O 1s orbital splitting and b) Cr 2p orbital splitting of CrVO$_4$ powder.

explained by Makuła et al. [65], the Kubelka-Munk function can be used in the analysis of the Tauc plot to find the optical band gap. Hence, the final equation used below is

$$[F(R) \cdot h\nu]^{1/\lambda} = B(h\nu - E_g) \qquad (4)$$

It must be noted that the function for a direct transition semiconductor is used to obtain the Tauc plot, as it shows the best fit for a straight line to make an intercept in Fig. 5, graphs (B) and (C). The optical band gap energy of the CrVO$_4$ material in its prepared state is estimated to be 2.35 eV; see Fig. 5(B), which is in agreement with other reports [67,68]. However, the part of the curve in Fig. 5(C) corresponding to the shoulder absorption peak gives another transition at 1.58 eV.

The XPS analysis confirms the presence of Cr, V, and O elements, revealing that the atomic percentage of V is higher than Cr in the composition, as shown in Fig. S10 (A) in the supplementary file. With respect to their penetration depths, XPS is surface sensitive whereas EDS analysis can be considered a volume sensitive method due to particle size in this case. The adventitious C 1 s peak at 284.8 eV corresponding to the C-C binding energy was used as the binding energy reference, whereas its presence problematizes the interpretation of this spectral band. The carbon peak components correspond to a mixed signal from the contamination on the surface and the eventual carbon signal from the material in Fig. S10 (B). Therefore, it is presented in the supplementary file without further analysis and discussion. Fig. 6(B) depicts the deconvoluted Cr 2p spectra exhibiting two main valence states of chromium: Cr^{3+} is manifested at 573.3 eV, 576.6 eV and Cr^{6+} at 578.6 eV. The Cr 2p shows two multiplet-split components for Cr^{3+} in Fig. 6(B), which lack usual resolution and instead display a much broadened band (expressed in terms of the full width at half maximum (FWHM) value) caused by the presence of unpaired d electrons [69,70]. Similarly, various oxidation states of V 2p are exposed during the formation of CrVO$_4$, indicating a strong hybridization between V 2p and O 1 s states exhibiting a broadened peak of the V 2p. The binding energies of V 2p3/2 are as follows: 515.7 eV for the V^{3+} peak, 516.6 eV and 518.0 eV for the V^{4+} peaks, and 518.5 eV for the V^{5+} peak (Fig. 6 (A)). In the literature, the O 1 s peak at 532.8 eV in Fig. 6(a) is a noted signature of the lattice oxygen present on the surface [71]. The ratio of the surface atomic Cr/V is approximately 9:14, possibly due to the slightly higher surface enrichment of the V atomic species. The outcome of XRD and EDS revealed that the major volume crystalline phase is monoclinic CrVO$_4$ with 1:1 Cr to V stoichiometry requiring chromium and vanadium in states Cr^{3+} and V^{5+} to be predominantly built in the cores of the particles, as expected in the synthesis up to 700 °C according to the
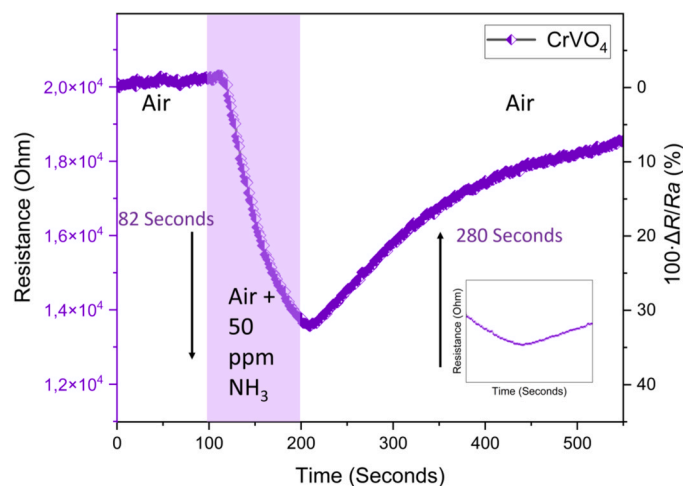

Fig. 7. An exemplary transient response curve of optimal sensing at operating temperature (330 °C) expressed using both the resistance values and percent change. The direct electrical resistance response of the sensor is on the left y-scale, whereas the right scale allows to follow the changes quantified in terms of the relative response (100·$\Delta R/Ra$).

literature [72–74]. The XPS analyses revealed that the surface of the particles was composed of a plethora of mixed valence states of both contained metal elements, possibly caused by their unsaturated bonding spheres and interactions with the adventitious carbon contaminations, oxygen, and moisture. Differently from chromium vanadate, these species could be associated with the low energy peak at 700 nm in the reflectance spectrum in Fig. 5. Nevertheless, it can be expected that the surface layer is responsible for the interaction with the analyte gas and that the surface quality is improved when the sensor is conditioned and operated at high temperatures.

3.2. Gas sensing studies

A preliminary screening of sensor responses was performed at various operating temperatures, and the results are given in the supplementary document in Fig. S11 and the associated paragraph. The minimum temperature for the sensor operation yielding a measurable response with no significant recovery was 250 °C, so moisture and humidity cross-sensitivity was not investigated. The sensor also showed
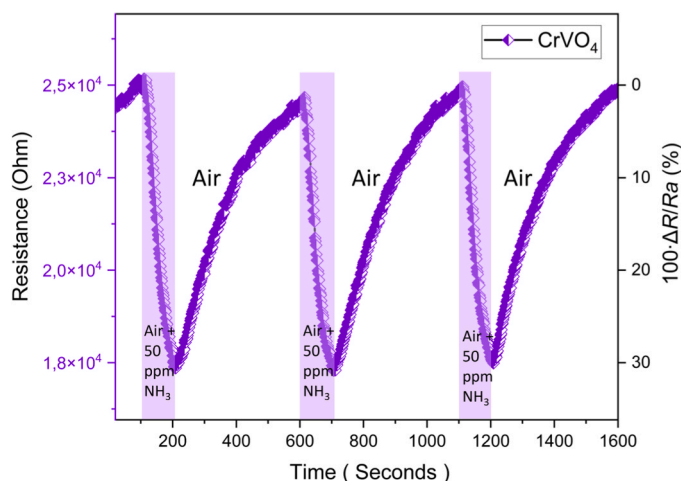
Fig. 8. Transient response curve of sensor repeatability expressed in terms of both the resistance values and percent change towards 50 ppm of NH_3 target gas in the synthetic air carrier gas. Recorded at the optimum operating temperature of 330 °C. The direct electrical resistance response of the sensor is on the left y-scale, whereas the right scale allows to follow the changes quantified in terms of the relative response ($100 \cdot \Delta R/Ra$).
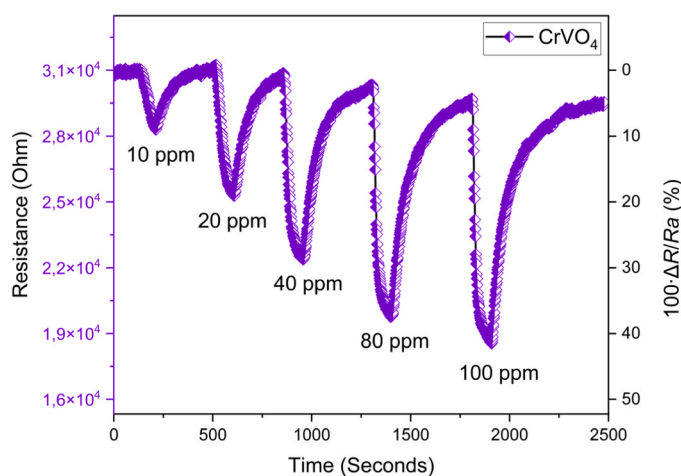

Fig. 9. Dynamic sensing characteristics expressed using both the resistance values and percent change to different concentrations of NH_3 at the optimum operating temperature of 330 °C. The direct electrical resistance response of the sensor is on the left y-scale, whereas the right scale allows to follow the changes quantified in terms of the relative response ($100 \cdot \Delta R/Ra$).

erratic behaviour beyond 450 °C as a result of instability in a baseline and reduced relative response. The optimal working temperature was determined to be 330 °C taking into account the higher relative response values, faster response and recovery times of the sensor towards 50 ppm NH_3 injections with the consistent 200 sccm gas flow rate.

Fig. 7 illustrates the CrVO$_4$ sensor reaction to a gas injection of 50 ppm of NH_3 for 100 s at 330 °C: it gives a relative response of 32% with 82 s for T 90 response time and 280 s for T 90 recovery time. This extended response and recovery time for the reaction could be attributed to the lack of nanostructuring and possibly high work potential requirements [47,75,76]. Effective surface adsorption/desorption cycles typically require adequate surface energy to exhibit rapid kinetics.

Fig. 8 illustrates that the CrVO$_4$ sensor response remained constant during three cycles of 50 ppm NH_3 gas infusion with similar T-90 response and recovery times around 83 s and 325 s at 330 °C and the consistent 200 sccm gas flow rate. This outcome suggests that the aforementioned material exhibited favorable recovery, consistency, and
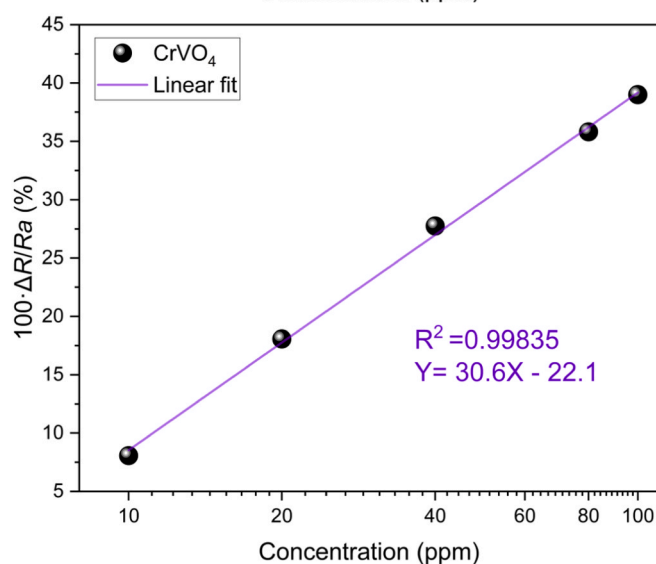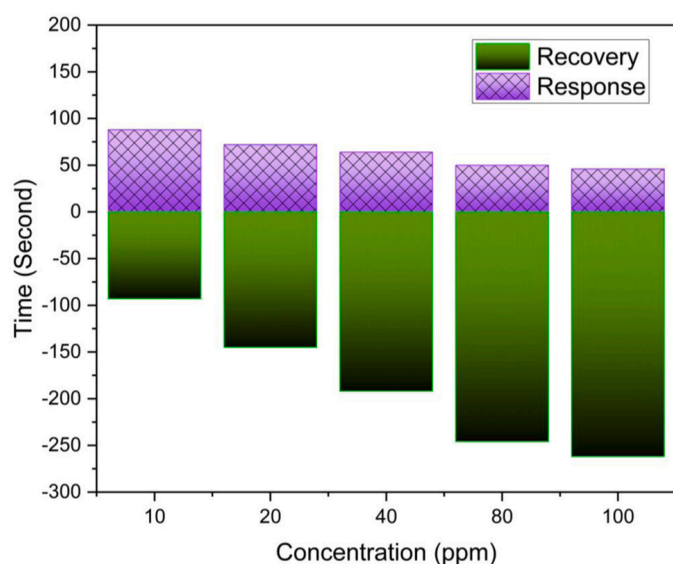

Fig. 10. (a) Response/recovery dynamics for various NH_3 concentrations (b) Logarithmic dependency of the relative response ($100 \cdot \Delta R/Ra$) of the CrVO$_4$ sensor depicted below.

thus rendering it appropriate for utilization. This may be driven by the nanosize effect as well as the lattice structure, which allows more oxygen vacancies [77,78].

The LOD value of the CrVO$_4$ sensor was determined by evaluating the isothermal dynamic response towards 10, 20, 40, 80, and 100 ppm NH_3 injections shown in Fig. 9. In accordance with our system design, a greater flow rate of 800 sccm was employed to obtain low target gas concentrations in this measurement. Baseline drift was noted related to the change in flow rate intended to dilute the target gas.

In Fig. 10(a), the calculated T-90 response and T-90 recovery times are shown. As the concentration of the target gas (NH_3) increases, it exhibits the predicted pattern of faster T-90 response and slower T-90 recovery times. This trend is observed across the gas concentration range from 10 ppm to 100 ppm. It usually depicts a possibly cascading reaction with the increased presence of target gas, which is able to easily react with the surface material. However, the extended recovery time could possibly be credited to gas molecules deeply trapped in active bonding sites as similar trend mentioned in this work [79]. The recovery time can be further improved by smaller nanoparticle size or employing different measurement techniques [80–82]. A calibration curve created using the experimental data is shown in Fig. 10(b). A linear relationship
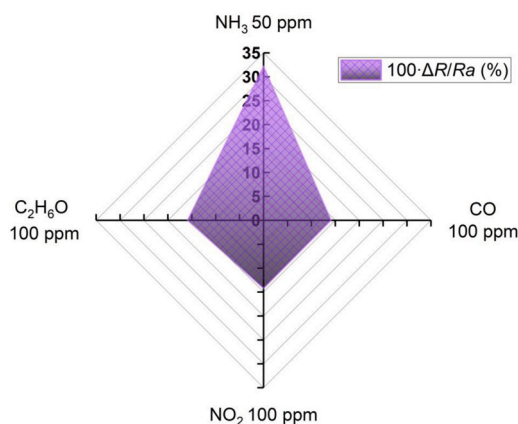
Fig. 11. Results of the cross-sensitivity testing for CrVO₄ sensor. The tested gases are indicated at each axis of the radar plot. The scale is identical for all axes.

between the relative response and the logarithm of concentration of NH₃ gas is seen in the graph. It shows a good linear fit to the equation Y = 30.6X + 8.53, with the high R² value of 0.99835. In other words, the sensor response shows logarithmic growth with increasing concentration, at least in the examined range of experimental conditions. Although the logarithmic growth model is a suitable mathematical description for the examined range, asymptotic exponential growth will be an appropriate model, if sensor saturation is observed for higher concentrations.

The response to the lowest tested ammonia concentration was analyzed further, as shown in the supplementary document in Fig. S13. The response peak, when analyzing the LOD of the prepared sensor (10 ppm), exceeds by far the generally accepted minimum value of the signal-to-noise ratio (n = 3σ). This allows us the conslusion that its real LOD might be much lower than the one detected in this work, as the reported value is limited by the used gas sensing system using gas cylinders of specific concentrations and given flow controllers. From the signal-to-noise ratio, it can be estimated that ca 0.7 ppm of target gas (as the signal for 10 ppm corresponds to about 39σ) is the point at which a clear distinction could be made from baseline noise. To the best of our knowledge, this LOD is comparable to, or better than the best values reported in the literature, namely [31] as mentioned in the introduction. In addition, the CrVO₄ syntheised in this work contains no noble elements and can be synthesised in a simple way.

The subsequent evaluation of the data shown in Fig. 11 included the cross-sensitivity test utilizing the current setup and experimental conditions using 330 °C as the operating temperature with flow rate set to 200 sccm to obtain the best response to the target gas. To establish the selectivity profile of CrVO₄ sensor, the dynamic response profiles towards various gases were examined using the same injection time 100 s. The compared concentration values of test gases were 50 ppm of NH₃, 100 ppm of C₂H₆O, 100 ppm of NO₂, and 100 ppm of CO. The prepared sensor was highly selective to the target gas NH₃; the response to the other gases, even when tested at double concentrations, was at best near half of the response to the target gas. Considering different concentrations of tested gases, the selectivity factor was calculated to be 4.2 against ethanol, 4.5 against NO₂ and 4.5 against CO for the same flow rate. It is calculated by multiplying the ratio of the relative response of our target gas and its gas concentration with the ratio of the relative response and gas concentration of the competing gas. Weaker electron-donating capacity was credited with explaining the relatively lower response to the other tested gases.

3.3. Sensing mechanism

The current study discusses a potential ammonia gas sensing

mechanism for the CrVO₄. The resistance of our material decreases in the presence of a reducing gas such as NH₃, which is typical for *n*-type semiconductors. On the other hand, orthorhombic CrVO₄ was previously reported to have *p*-type electrical conductivity [83]. No report on conductivity type of monoclinic CrVO₄ is available according to our best knowledge. Nevertheless, semiconductor surfaces were shown to switch between conductivity types due to certain reasons, such as pressure, doping, surface modification, defect formation, and exposition to the analyte gas, irreversible as well as even reversible changes were reported [84–87]. A reason that helps us better understand the conduction mechanism of the material prepared in this work is the band bending induced by oxygen species adsorption and formation of the surface inversion layer [88].

The crystal structure of CrVO₄ strongly influences its characteristics; how the atoms are arranged in the lattice determines the electrical band structure. As VO₄ tetrahedra connect with the Cr₄O₁₆ clusters in the monoclinic structure, an extensive network is created [89]. As mentioned above, the presence of bridging O in the better-positioned V - O - Cr bond in the crystal structure could possibly be responsible for less steric hindrance and lower adsorption energy for adsorbing oxygen anions and target gases [90].

The literature provides limited information about the high-temperature electrical characteristics of CrVO₄-type orthovanadates that contain cations with filled electron configurations. Hence, it is difficult to make final conclusions by comparing these orthovanadates with other transition metal compounds [83]. The dielectric and conduction processes may have separate effects in addition to the participation of electrons owing to valence fluctuation because of the substantial number of vacant spaces and severely deformed polyhedral units in the lattice of CrVO₄-type structures [91,92].

The general working principle of nanomaterials was described by Barsan et al. [93]. It was demonstrated that many conduction mechanisms can be involved in the sensing mechanism. There is also the possibility of the mean free path of the free charge carriers being comparable with the dimension of the nanoparticle. The surface of the studied material can contribute in various manners to the conduction mechanism due to its local variation in properties as the material has imperfectly sintered larger grains, small grains, and narrow necks of variable diameter. Nevertheless, the surface quality and energy band bending are assumed to play a major role in the sensing mechanism of the studied material.

According to the literature [93], the surface of the material has surface coverage by active oxygen species influencing the hole concentration when operated in air and at higher temperatures. At the working temperature of 330 °C, the dominant oxygen species adsorbed on the surface are O⁻ ions, which cause energy band bending [94]. It can be presumed that the NH₃ gas molecules, when injected into the gas sensing system, come into contact with the surface, and the NH₃ reacts with the O⁻-rich surface, which is manifested as a decrease in the overall resistance of the sensor. The presence of exposed reducing gas leads to a partial consumption of pre-adsorbed oxygen ions on the surface of the sensitive film. This interaction reduces the concentration of electrons in the surface layer, so the resistance of the material decreases, while in the recovery process, the shift in the reaction towards removing NH₃ being replaced by O⁻ again increases the resistance to the baseline level.

Changes in charge carrier concentration on the surface of the material induce changes in the electron affinity (χ) band bending (qV) and the work function (φ) of the sensing material. These factors modify the electronic structure of the material and the change of band bending (qΔV) can be calculated from the sensing performance (in terms of observed resistance changes) of the sensor [95] and get Eq. 5 below.

$$q\Delta V = -2k_B T \ln\left(\frac{R_G}{R_A}\right) \tag{5}$$

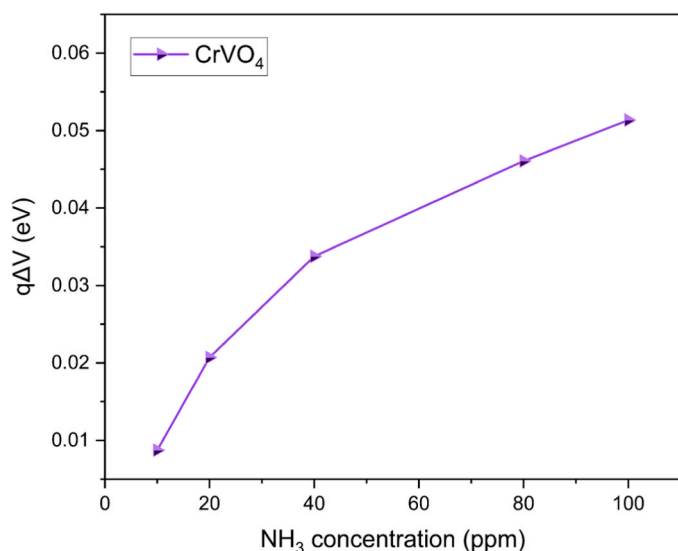where k_B is the Boltzmann constant, T is the temperature, R_G is the

Fig. 12. The change in $q\Delta V$ over NH_3 concentration for the CrVO$_4$ sensor.

sensor resistance in gas, and R_A is the sensor resistance in air. The value of $q\Delta V$ was computed in relation to the sensor response to varied NH_3 gas concentrations, and the resulting plot is shown in Fig. 12. The band bending shows a logarithmic growth shape or possibly an asymptotic exponential growth as saturation at high analyte concentration that can be reasonably expected. It correlates well with the calibration dependency of the sensor response on the ammonia concentration in Fig. 10 (b).

The surface reactions and mutual interactions of adsorbed species influence the surface conductivity due to changes in the charge density in the depletion layer on the surface of the material grains and the consequent decrease in the band bending qV. The positive value of $q\Delta V$ indicates a decrease of the band bending qV and a shift of the Fermi level (E_F) towards higher values, as illustrated in Fig. 13. The schematisation of the sensing principle is based on an analogy with the literature related

to our specific operating temperature conditions, gas compositions and concentrations, and plausible surface effects [96–99].

To summarize, the reported bimetal chromium orthovanadate material exhibited significant sensitivity, LOD, and selectivity, demonstrating its potential for applications sensing ammonia gas in ppm concentrations. Moreover, we contributed to understanding of the sensing mechanism, although further and more profound instrumented studies will be necessary to clarify the mechanisms fully.

4. Conclusions

Chromium orthovanadate nanostructures were fabricated in this work using the co-precipitation technique. A polycrystalline CrVO$_4$ structure of a monoclinic system belonging to the space group C2/m was identified as the prevailing phase, followed by traces of $(Cr_xV_{1-x})_2O_3$ in the trigonal crystal system and minor surface amorphous contaminations. The particle size and surface morphology are seen as nanoparticles aggregated from nanocrystallites and agglomerated to form larger particles. The chemiresistive sensor made from as-prepared nanostructures had the maximum response of 32% relative change in resistance when employed towards 50 ppm of NH_3 gas in the air. The lowest experimentally recorded response of the CrVO$_4$ sensor towards 10 ppm of NH_3 gas allowed the estimation of the limit of detection (LOD) ca 0.7 ppm using the signal-to-noise 3σ ratio method. The LOD is at least comparable or better than what can be found in contemporary literature. However, the material prepared in this work achieves good sensing properties without the use of noble elements. The highest tested concentration of 100 ppm also induced a significant response. The linear fit of the sensor response in dependence on the logarithm of the analyte concentration demonstrated no sign of saturation, verifying thus the wide concentration range of the sensor's applicability. In the cross-sensitivity testing, the sensor shows upto 4.5 higher sensitivity to ammonia than to other gasses (CO, NO_2, EtOH). As the optimum temperature for the sensor operation is 330 °C, the moisture and humidity do not put in question its use outside the laboratory conditions. These findings support the ability of the CrVO$_4$ nanomaterial to provide reliable selective NH_3 gas sensing that is inexpensive and simple to manufacture. It was demonstrated that the material is worth of future research
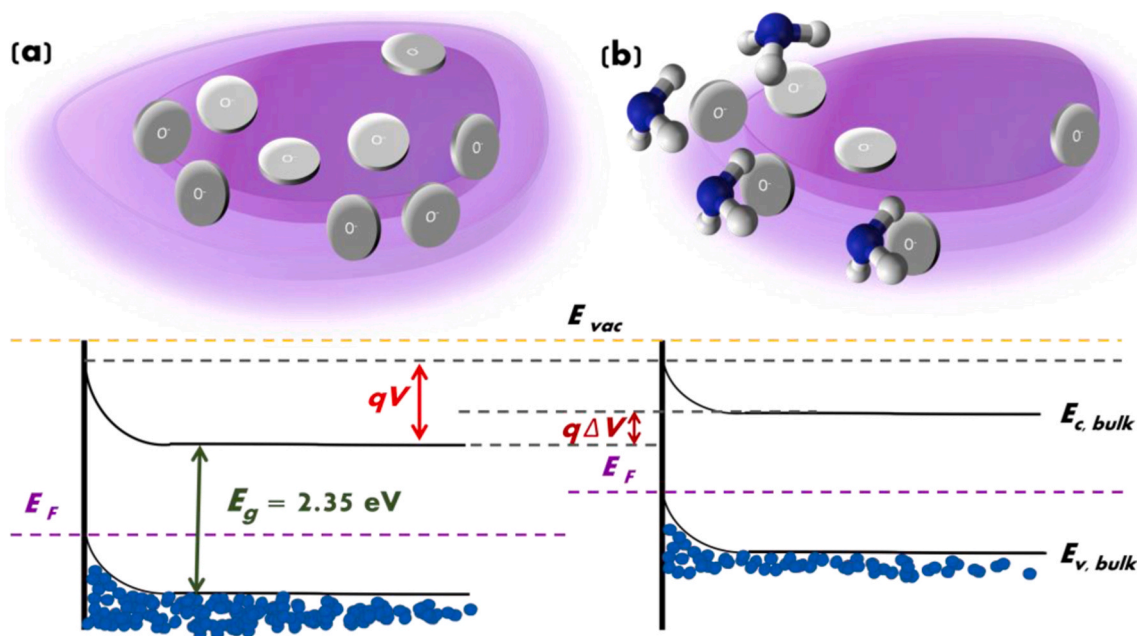

Fig. 13. Band bending (a) in the presence of solely oxygen species from the air atmosphere (b) in the presence of ammonia admixed in the air atmosphere towards the CrVO$_4$ sensor. $E_{c,bulk}$ and $E_{v,\,bulk}$ indicate the valence and conduction band edge energy levels in bulk, respectively. E_{vac} indicates the vacuum level, E_F stands for Fermi level and E_g indicates the forbidden gap energy. The band bending is denoted as qV, and the change of the band bending is indicated by $q\Delta V$.

interest, related especially to its long-term stability, repeatability, structural alterations and doping investigations.

CRediT authorship contribution statement

Declaration of Competing Interest

The authors declare that they have no known competing financial interests or personal relationships that could have appeared to influence the work reported in this paper.

Data Availability

Data will be made available on request.

Acknowledgement

Appendix A. Supporting information

Supplementary data associated with this article can be found in the online version at doi:10.1016/j.snb.2024.135380.

References

[1] N. Tamaekong, C. Liewhiran, A. Wisitsoraat, S. Phanichphant, Flame-spray-made undoped zinc oxide films for gas sensing applications, Sensors 10 (2010) 7863–7873, https://doi.org/10.3390/s100807863.

[2] A.G. Shrivas, R.G. Bavane, A.M. Mahajan, Electronic nose: a toxic gas sensor by polyaniline thin film conducting polymer, in: International Workshop on Physics of Semiconductor Devices, 2007, IEEE, 2007, pp. 621–623, https://doi.org/10.1109/IWPSD.2007.4472595.

[3] S.-J. Kim, I.-S. Hwang, Y.C. Kang, J.-H. Lee, Design of selective gas sensors using additive-loaded In$_2$O$_3$ hollow spheres prepared by combinatorial hydrothermal reactions, Sensors 11 (2011) 10603–10614, https://doi.org/10.3390/s111110603.

[4] I.-C. Chen, S.-S. Lin, T.-J. Lin, C.-L. Hsu, T.J. Hsueh, T.-Y. Shieh, The assessment for sensitivity of a NO$_2$ gas sensor with ZnGa$_2$O$_4$/ZnO core-shell nanowires—a novel approach, Sensors 10 (2010) 3057–3072, https://doi.org/10.3390/s100403057.

[5] A. Fuerte, R.X. Valenzuela, M.J. Escudero, L. Daza, Ammonia as efficient fuel for SOFC, J. Power Sources 192 (2009) 170–174, https://doi.org/10.1016/j.jpowsour.2008.11.037.

[6] L. Zhang, W. Yang, Direct ammonia solid oxide fuel cell based on thin proton-conducting electrolyte, J. Power Sources 179 (2008) 92–95, https://doi.org/10.1016/j.jpowsour.2007.12.061.

[7] A.S. Chellappa, C.M. Fischer, W.J. Thomson, Ammonia decomposition kinetics over Ni-Pt/Al$_2$O$_3$ for PEM fuel cell applications, Appl. Catal. A Gen. 227 (2002) 231–240, https://doi.org/10.1016/S0926-860X(01)00941-3.

[8] T. Hejze, J.O. Besenhard, K. Kordesch, M. Cifrain, R.R. Aronsson, Current status of combined systems using alkaline fuel cells and ammonia as a hydrogen carrier, J. Power Sources 176 (2008) 490–493, https://doi.org/10.1016/j.jpowsour.2007.08.117.

[9] M. Comotti, S. Frigo, Hydrogen generation system for ammonia–hydrogen fuelled internal combustion engines, Int J. Hydrog. Energy 40 (2015) 10673–10686, https://doi.org/10.1016/j.ijhydene.2015.06.080.

[10] R. Lan, J.T.S. Irvine, S. Tao, Ammonia and related chemicals as potential indirect hydrogen storage materials, Int J. Hydrog. Energy 37 (2012) 1482–1494, https://doi.org/10.1016/j.ijhydene.2011.10.004.

[11] G.K. Mani, J.B.B. Rayappan, Selective detection of ammonia using spray pyrolysis deposited pure and nickel doped ZnO thin films, Appl. Surf. Sci. 311 (2014) 405–412, https://doi.org/10.1016/j.apsusc.2014.05.075.

[12] M. Chatain, E. Chretien, S. Crunaire, E. Jantzem, Road traffic and its influence on urban ammonia concentrations (France), Atmosphere 13 (2022) 1032, https://doi.org/10.3390/atmos13071032.

[13] M. Pandolfi, F. Amato, C. Reche, A. Alastuey, R.P. Otjes, M.J. Blom, X. Querol, Summer ammonia measurements in a densely populated Mediterranean city, Atmos. Chem. Phys. 12 (2012) 7557–7575, https://doi.org/10.5194/acp-12-7557-2012.

[14] Y.S. Tang, C.R. Flechard, U. Dämmgen, S. Vidic, V. Djuricic, M. Mitosinkova, H.T. Uggerud, M.J. Sanz, I. Simmons, U. Dragosits, E. Nemitz, M. Twigg, N. van Dijk, Y. Fauvel, F. Sanz, M. Ferm, C. Perrino, M. Catrambone, D. Leaver, C.F. Braban, J.N. Cape, M.R. Heal, M.A. Sutton, Pan-European rural monitoring network shows dominance of NH$_3$ gas and NH$_4$NO$_3$ aerosol in inorganic atmospheric pollution load, Atmos. Chem. Phys. 21 (2021) 875–914, https://doi.org/10.5194/acp-21-875-2021.

[15] M.M. Twigg, A.J.C. Berkhout, N. Cowan, S. Crunaire, E. Dammers, V. Ebert, V. Gaudion, M. Haaima, C. Häni, L. John, M.R. Jones, B. Kamps, J. Kentisbeer, T. Kupper, S.R. Leeson, D. Leuenberger, N.O.B. Lüttschwager, U. Makkonen, N.A. Martin, D. Missler, D. Mounsor, A. Neftel, C. Nelson, E. Nemitz, R. Oudwater, C. Pascale, J.-E. Petit, A. Pogany, N. Redon, J. Sintermann, A. Stephens, M.A. Sutton, Y.S. Tang, R. Zijlmans, C.F. Braban, B. Niederhauser, Intercomparison of in situ measurements of ambient NH$_3$: instrument performance and application under field conditions, Atmos. Meas. Tech. 15 (2022) 6755–6787, https://doi.org/10.5194/amt-15-6755-2022.

[16] H. Guo, R. Otjes, P. Schlag, A. Kiendler-Scharr, A. Nenes, R.J. Weber, Effectiveness of ammonia reduction on control of fine particle nitrate, Atmos. Chem. Phys. 18 (2018) 12241–12256, https://doi.org/10.5194/acp-18-12241-2018.

[17] European Environmental Agency (EEA), Air quality in Europe 2022. Report no. 05/2022., 2022. ⟨https://doi.org/10.2800/488115⟩.

[18] Air Breizh, Ministère De La Transition Écologique, L'ammoniac - Air Breizh, (n.d.). ⟨https://www.airbreizh.asso.fr/air-exterieur/les-polluants/lammoniac/⟩ (accessed June 2, 2023).

[19] L. Liu, X. Zhang, A.Y.H. Wong, X. Wu, X. Liu, Y. Li, H. Mi, X. Lu, L. Zhao, Z. Wang, X. Wu, J. Wei, Estimating global surface ammonia concentrations inferred from satellite retrievals, Atmos. Chem. Phys. 19 (2019) 12051–12066, https://doi.org/10.5194/ACP-19-12051-2019.

[20] J.E. Ellis, A. Star, Carbon nanotube based gas sensors toward breath analysis, Chempluschem 81 (2016) 1248–1265, https://doi.org/10.1002/CPLU.201600478.

[21] X. Zhou, Z. Xue, X. Chen, C. Huang, W. Bai, Z. Lu, T. Wang, Nanomaterial-based gas sensors used for breath diagnosis, J. Mater. Chem. B 8 (2020) 3231–3248, https://doi.org/10.1039/C9TB02518A.

[22] S.Y. Yu, T.W. Tung, H.Y. Yang, G.Y. Chen, C.C. Shih, Y.C. Lee, C.C. Chen, H.W. Zan, H.F. Meng, C.J. Lu, C.L. Wang, W. Bin Jian, O. Soppera, A versatile method to enhance the operational current of air-stable organic gas sensor for monitoring of breath ammonia in hemodialysis patients, ACS Sens 4 (2019) 1023–1031, https://doi.org/10.1021/acssensors.9b00223.

[23] Z. Bielecki, T. Stacewicz, J. Smulko, J. Wojtas, Ammonia gas sensors: comparison of solid-state and optical methods, 2020, Appl. Sci. Vol. 10 (2020) 5111, https://doi.org/10.3390/APP10155111.

[24] W.A. Groves, D. Agarwal, M.J. Chandra, S.J. Reynolds, Evaluation of a fluorometric method for measuring low concentrations of ammonia in ambient air, J. Environ. Monit. 7 (2005) 163–168, https://doi.org/10.1039/B411109E.

[25] B. Timmer, W. Olthuis, A. Van Den Berg, Ammonia sensors and their applications—a review, Sens Actuators B Chem. 107 (2005) 666–677, https://doi.org/10.1016/J.SNB.2004.11.054.

[26] M. Meyyappan, Carbon nanotube-based chemical sensors, Small 12 (2016) 2118–2129, https://doi.org/10.1002/SMLL.201502555.

[27] L. Filipovic, S. Selberherr, Application of two-dimensional materials towards CMOS-integrated gas sensors, 12, Nanomaterials Vol. 12 (2022) 3651, https://doi.org/10.3390/NANO12203651.

[28] C.F. Li, C.Y. Hsu, Y.Y. Li, NH3 sensing properties of ZnO thin films prepared via sol–gel method, J. Alloy. Compd. 606 (2014) 27–31, https://doi.org/10.1016/J.JALLCOM.2014.03.120.

[29] I. Rawal, Facial synthesis of hexagonal metal oxide nanoparticles for low temperature ammonia gas sensing applications, RSC Adv. 5 (2014) 4135–4142, https://doi.org/10.1039/C4RA12747A.

[30] A. Bhardwaj, I.H. Kim, L. Mathur, J.Y. Park, S.J. Song, Ultrahigh-sensitive mixed-potential ammonia sensor using dual-functional NiWO4 electrocatalyst for exhaust environment monitoring, J. Hazard. Mater. 403 (2021), https://doi.org/10.1016/j.jhazmat.2020.123797.

[31] F.U. Khan, S. Mehmood, X. Zhao, Y. Yang, X. Pan, Ultra-sensitive bimetallic alloy loaded with porous architecture MOF for ammonia detection at room temperature. Proceedings - IEEE International Symposium on Circuits and Systems, Institute of Electrical and Electronics Engineers Inc, 2021, https://doi.org/10.1109/ISCAS51556.2021.9401554.

[32] N. Garg, M. Kumar, N. Kumari, A. Deep, A.L. Sharma, Chemoresistive room-temperature sensing of ammonia using zeolite imidazole framework and reduced graphene oxide (ZIF-67/ RGO) composite, ACS Omega 5 (2020) 27492–27501, https://doi.org/10.1021/acsomega.0c03981.

[33] W. Jiao, J. He, L. Zhang, Synthesis and high ammonia gas sensitivity of (CH3NH3) PbBr3−xIx perovskite thin film at room temperature, Sens. Actuators B Chem. 309 (2020), https://doi.org/10.1016/j.snb.2020.127786.

[34] X. Wang, Y. Zhou, J. Luo, F. Sun, J. Zhang, Synthesis of V-doped urchin-like NiCo2O4 with rich oxygen vacancies for electrocatalytic oxygen evolution reactions, Electrochim. Acta 406 (2022) 139800, https://doi.org/10.1016/J.ELECTACTA.2021.139800.

[35] P. Wisesa, C. Li, C. Wang, T. Mueller, Materials with the CrVO4 structure type as candidate superprotonic conductors, RSC Adv. 9 (2019) 31999–32009, https://doi.org/10.1039/C9RA06291B.

[36] L. Shreenivasa, R.T. Yogeeshwari, R. Viswanatha, K. Yogesh, S. Ashoka, Sucrose-assisted rapid synthesis of multifunctional CrVO4 nanoparticles: a new high-performance cathode material for lithium ion batteries, Ionics 27 (2021) 39–48, https://doi.org/10.1007/S11581-020-03783-3.

[37] G. Bera, A. Mishra, P. Mal, A. Sankarakumar, P. Sen, A. Gangan, B. Chakraborty, V. R. Reddy, P. Das, G.R. Turpu, Multifunctionality of partially reduced graphene oxide-CrVO4 nanocomposite: electrochemical and photocatalytic studies with theoretical insight from density functional theory, J. Phys. Chem. A 122 (2018) 21140–21150, https://doi.org/10.1021/acs.jpcc.8b05291.

[38] T.H. Gayathri, A.A. Yaremchenko, K. Zakharchuk, J. James, Effect of magnesium addition on the structural, microstructural and electrical properties of YVO4, J. Alloy. Compd. 672 (2016) 549–557, https://doi.org/10.1016/J.JALLCOM.2016.02.210.

[39] Y.V. Kaneti, Z. Zhang, J. Yue, X. Jiang, A. Yu, Porous FeVO4 nanorods: synthesis, characterization, and gas-sensing properties toward volatile organic compounds, J. Nanopart. Res. 15 (2013) 1–15, https://doi.org/10.1007/S11051-013-1948-Z.

[40] Y. Liu, M. Zhang, L. Yang, Z. Wu, Z. Li, Preparation of CeVO4 with VO2 as precursor performing high selectivity and sensitivity to ammonia, J. Alloy. Compd. 909 (2022) 164666, https://doi.org/10.1016/J.JALLCOM.2022.164666.

[41] Y. Shuai, R. Peng, Y. He, X. Liu, X. Wang, W. Guo, NiO/BiVO4 p-n heterojunction microspheres for conductometric triethylamine gas sensors, Sens. Actuators B Chem. 384 (2023) 133625, https://doi.org/10.1016/J.SNB.2023.133625.

[42] S. Liu, F. Hu, J. Zhang, H. Tang, M. Shao, Surface-doping effect of InVO4 nanoribbons and the distinctive behavior as gas sensors, ACS Appl. Mater. Interfaces 5 (2013) 3208–3211, https://doi.org/10.1021/am400221p.

[43] C. Wang, Y. He, H. Liu, B. Yang, J. Wang, H. Yu, F. Xia, J. Xiao, Potentiometric sensor based on chromium vanadate sensing electrode for high temperature ammonia detection, J. Electrochem. Soc. 168 (2021) 047510, https://doi.org/10.1149/1945-7111/ABF4B1.

[44] Y. Wang, J. Liu, X. Cui, Y. Gao, J. Ma, Y. Sun, P. Sun, F. Liu, X. Liang, T. Zhang, G. Lu, NH3 gas sensing performance enhanced by Pt-loaded on mesoporous WO3, Sens. Actuators B Chem. 238 (2017) 473–481, https://doi.org/10.1016/j.snb.2016.07.085.

[45] B. Lan, C. Tang, L. Chen, W. Zhang, W. Tang, C. Zuo, X. Fu, S. Dong, Q. An, P. Luo, FeVO4·nH2O@rGO nanocomposite as high performance cathode materials for aqueous Zn-ion batteries, J. Alloy. Compd. 818 (2020) 153372, https://doi.org/10.1016/J.JALLCOM.2019.153372.

[46] Q. Albert G. David F. Robert F. Thomas V. Hans B. Sara B. Ausrine M. Sanjay LaFeO3 Nanofibers for High Detection of Sulfur-Containing Gases ACS Publ. 7 2019 6023 6032 doi: 10.1021/ACSSUSCHEMENG.8B06132.

[47] K.J. Choi, H.W. Jang, One-dimensional oxide nanostructures as gas-sensing materials: review and issues, Sensors 10 (2010) 4083–4099, https://doi.org/10.3390/s100404083.

[48] T. Oyama, Y. Iimura, K. Takeuchi, T. Ishii, Synthesis of (CrxV1−x)2O3 fine particles by a laser-induced vapor-phase reaction and their crystal structure, J. Mater. Sci. 34 (1999) 439–444, https://doi.org/10.1023/A:1004517906572.

[49] Tetsuya Shishido, Preparation of crystalline CrVO4 catalyst by soft chemistry technique and application for vapor-phase oxidation of picolines, J. Jpn. Pet. Inst. 54 (2011) 225–236, https://doi.org/10.1627/jpi.54.225.

[50] Y. RT, S. N, S. L, A. Khosla, M. C, A. S, Synthesis, characterization and oer performance of CrVO4 nanoparticles, ECS Trans. 107 (2022) 14335–14342, https://doi.org/10.1149/10701.14335ecst.

[51] F. Jiang, S. Deng, L. Niu, G. Xiao, Effect of supports on the structure and activity of vanadium-chromium oxide catalysts for ammoxidation of 3-picoline, Chin. J. Catal. 34 (2013) 1833–1838, https://doi.org/10.1016/s1872-2067(12)60650-0.

[52] Y.V. Kaneti, Z. Zhang, J. Yue, X. Jiang, A. Yu, Porous FeVO4 nanorods: synthesis, characterization, and gas-sensing properties toward volatile organic compounds, J. Nanopart. Res. 15 (2013) 1–15, https://doi.org/10.1007/S11051-013-1948-Z.

[53] S. Alagarsamy, R.K. Devi, T.-W. Chen, S.-M. Chen, B.-S. Lou, R. Ramachandran, A. M. Al-Mohaimeed, M.F. El-Tohamy, M.S. Elshikh, J. Yu, R.-H. Li, Chromium vanadate nanoparticles entrapped reduced graphene oxide nanosheets: a nanocomposite with high catalytic activity for the detection of hypertension-drug nifedipine in biological samples, Colloids Surf. A Physicochem. Eng. Asp. 674 (2023) 131903, https://doi.org/10.1016/j.colsurfa.2023.131903.

[54] I. Khan, A. Qurashi, Shape controlled synthesis of copper vanadate platelet nanostructures, their optical band edges, and solar-driven water splitting properties, Sci. Rep. 7 (2017) 14370, https://doi.org/10.1038/s41598-017-14111-7.

[55] G. Kesavan, M. Pichumani, S.-M. Chen, Influence of crystalline, structural, and electrochemical properties of iron vanadate nanostructures on flutamide detection, ACS Appl. Nano Mater. 4 (2021) 5883–5894, https://doi.org/10.1021/acsanm.1c00802.

[56] L.M. Alrehaily, J.M. Joseph, A.Y. Musa, D.A. Guzonas, J.C. Wren, Gamma-radiation induced formation of chromium oxide nanoparticles from dissolved dichromate, Phys. Chem. Chem. Phys. 15 (2013) 98–107, https://doi.org/10.1039/C2CP43150E.

[57] T. Lehnen, M. Valldor, D. Nižňanský, S. Mathur, Hydrothermally grown porous FeVO4 nanorods and their integration as active material in gas-sensing devices, J. Mater. Chem. A Mater. 2 (2014) 1862–1868, https://doi.org/10.1039/C3TA12821K.

[58] G. Bera, V.R. Reddy, P. Rambabu, P. Mal, P. Das, N. Mohapatra, G. Padmaja, G. R. Turpu, Triclinic-monoclinic-orthorhombic (T-M-O) structural transitions in phase diagram of FeVO4-CrVO4 solid solutions, J. Appl. Phys. 122 (2017), https://doi.org/10.1063/1.4985793.

[59] A.M. Zhang, K. Liu, J.T. Ji, C.Z. He, Y. Tian, F. Jin, Q.M. Zhang, Raman phonons in multiferroic FeVO4 crystals, Chin. Phys. B 24 (2015), https://doi.org/10.1088/1674-1056/24/12/126301.

[60] H. Tian, I.E. Wachs, L.E. Briand, Comparison of UV and visible Raman spectroscopy of bulk metal molybdate and metal vanadate catalysts, J. Phys. Chem. B 109 (2005) 23491–23499, https://doi.org/10.1021/JP053879J.

[61] F.J. Manjón, P. Rodríguez-Hernández, A. Muñoz, A.H. Romero, D. Errandonea, K. Syassen, Lattice dynamics of YVO4 at high pressures, Phys. Rev. B Condens Matter Mater. Phys. 81 (2010) 075202, https://doi.org/10.1103/PHYSREVB.81.075202.

[62] P. Botella, S. López-Moreno, D. Errandonea, F.J. Manjón, J.A. Sans, D. Vie, A. Vomiero, High-pressure characterization of multifunctional CrVO4, J. Phys. Condens. Matter 32 (2020), https://doi.org/10.1088/1361-648X/ab9408.

[63] V. Panchal, S. López-Moreno, D. Santamaría-Pérez, D. Errandonea, F.J. Manjón, P. Rodríguez-Hernandez, A. Muñoz, S.N. Achary, A.K. Tyagi, Zircon to monazite phase transition in CeVO4: X-ray diffraction and Raman-scattering measurements, Phys. Rev. B Condens Matter Mater. Phys. 84 (2011) 024111, https://doi.org/10.1103/PHYSREVB.84.024111.

[64] V. Panchal, D. Errandonea, F.J. Manjón, A. Muñoz, P. Rodríguez-Hernández, S. N. Achary, A.K. Tyagi, High-pressure lattice-dynamics of NdVO4, J. Phys. Chem. Solids 100 (2017) 126–133, https://doi.org/10.1016/j.jpcs.2016.10.001.

[65] P. Makuła, M. Pacia, W. Macyk, How to correctly determine the band gap energy of modified semiconductor photocatalysts based on UV-vis spectra, J. Phys. Chem. Lett. 9 (2018) 6814–6817, https://doi.org/10.1021/acs.jpclett.8b02892.

[66] R. López, R. Gómez, Band-gap energy estimation from diffuse reflectance measurements on sol-gel and commercial TiO2: a comparative study, J. Solgel Sci. Technol. 61 (2012) 1–7, https://doi.org/10.1007/S10971-011-2582-9.

[67] G. Bera, A. Mishra, P. Mal, A. Sankarakumar, P. Sen, A. Gangan, B. Chakraborty, V. R. Reddy, P. Das, G.R. Turpu, Multifunctionality of partially reduced graphene oxide-CrVO4 nanocomposite: electrochemical and photocatalytic studies with theoretical insight from density functional theory, J. Phys. Chem. A 122 (2018) 21140–21150, https://doi.org/10.1021/acs.jpcc.8b05291.

[68] L. Zhou, D. Guevarra, J.M. Gregoire, High throughput discovery of enhanced visible photoactivity in Fe–Cr vanadate solar fuels photoanodes, J. Phys.: Energy 4 (2022) 044001, https://doi.org/10.1088/2515-7655/ac817e.

[69] R.P. Gupta, S.K. Sen, Calculation of multiplet structure of core p -vacancy levels. II, Phys. Rev. B 12 (1975) 15, https://doi.org/10.1103/PhysRevB.12.15.

[70] M.C. Biesinger, B.P. Payne, A.P. Grosvenor, L.W.M. Lau, A.R. Gerson, R.S.C. Smart, Resolving surface chemical states in XPS analysis of first row transition metals, oxides and hydroxides: Cr, Mn, Fe, Co and Ni, Appl. Surf. Sci. 257 (2011) 2717–2730, https://doi.org/10.1016/J.APSUSC.2010.10.051.

[71] X. Zhao, Y. Yan, L. Mao, M. Fu, H. Zhao, L. Sun, Y. Xiao, G. Dong, A relationship between the V4+/V5+ ratio and the surface dispersion, surface acidity, and redox performance of V2O5–WO3/TiO2 SCR catalysts, RSC Adv. 8 (2018) 31081–31093, https://doi.org/10.1039/C8RA02857E.

[72] G. Silversmit, D. Depla, H. Poelman, G.B. Marin, R. De Gryse, Determination of the V2p XPS binding energies for different vanadium oxidation states (V5+ to V0+), J. Electron Spectrosc. Relat. Phenom. 135 (2004) 167–175, https://doi.org/10.1016/J.ELSPEC.2004.03.004.

[73] A. Maetaki, M. Yamamoto, H. Matsumoto, K. Kishi, The preparation of ultra-thin chromium–vanadium oxides on Cu(100) studied by XPS and LEED, Surf. Sci. 445 (2000) 80–88, https://doi.org/10.1016/S0039-6028(99)01044-4.

[74] Y. Huang, T. Li, Q. You, X. You, Q. Zhang, D. Zhang, G. Xie, Solvothermal synthesis and characterization of nanocrystalline vanadium-chromium composite oxides and catalytic ammoxidation of 2,6-dichlorotoluene, Chin. J. Catal. 39 (2018) 1814–1820, https://doi.org/10.1016/S1872-2067(18)63119-5.

[75] A. Wei, L. Pan, W. Huang, Recent progress in the ZnO nanostructure-based sensors, Mater. Sci. Eng.: B 176 (2011) 1409–1421, https://doi.org/10.1016/j.mseb.2011.09.005.

[76] G. Jiménez-Cadena, J. Riu, F.X. Rius, Gas sensors based on nanostructured materials, Analyst 132 (2007) 1083–1099, https://doi.org/10.1039/B704562J.

[77] A. Kumar, M. Kumar, R. Kumar, R. Singh, B. Prasad, D. Kumar, Numerical modelling of chemisorption of oxygen gas molecules on the surface of semiconductor for gas sensors applications, Mater. Today Proc. 18 (2019) 1272–1279, https://doi.org/10.1016/J.MATPR.2019.06.589.

[78] A. Rothschild, Y. Komem, On the relationship between the grain size and gas-sensitivity of chemo-resistive metal-oxide gas sensors with nanosized grains, J. Electroceram. 13 (2004) 697–701, https://doi.org/10.1007/S10832-004-5178-8.

[79] M. Dun, J. Tan, W. Tan, M. Tang, X. Huang, CdS quantum dots supported by ultrathin porous nanosheets assembled into hollowed-out Co_3O_4 microspheres: a room-temperature H_2S gas sensor with ultra-fast response and recovery, Sens. Actuators B Chem. 298 (2019) 126839, https://doi.org/10.1016/J.SNB.2019.126839.

[80] R. Zhang, W. Pang, Z. Feng, X. Chen, Y. Chen, Q. Zhang, H. Zhang, C. Sun, J. J. Yang, D. Zhang, Enabling selectivity and fast recovery of ZnO nanowire gas sensors through resistive switching, Sens. Actuators B Chem. 238 (2017) 357–363, https://doi.org/10.1016/J.SNB.2016.07.068.

[81] N. Izu, S. Nishizaki, T. Itoh, M. Nishibori, W. Shin, I. Matsubara, Gas response, response time and selectivity of a resistive CO sensor based on two connected CeO_2 thick films with various particle sizes, Sens. Actuators B Chem. 136 (2009) 364–370, https://doi.org/10.1016/J.SNB.2008.12.018.

[82] N. Izu, W. Shin, I. Matsubara, N. Murayama, The effects of the particle size and crystallite size on the response time for resistive oxygen gas sensor using cerium oxide thick film, Sens. Actuators B Chem. 94 (2003) 222–227, https://doi.org/10.1016/S0925-4005(03)00330-7.

[83] T. Gro, H. Duda, J. Krok-kowalski, J. Walczak, E. Filipek, P. Tabero, A. Wyrostek, K. Barner, Electrical and optical properties of AVO_4 (A = Fe, Cr, Al) compounds, ⟨Http://Dx.Doi.Org/10.1080/10420159508226277⟩ 133 (2006) 341–348. ⟨https://doi.org/10.1080/10420159508226277⟩.

[84] J.H. Song, T. Akiyama, A.J. Freeman, Stabilization of bulk p-type and surface n-type carriers in Mg-doped InN {0001} films, Phys. Rev. Lett. 101 (2008) 186801, https://doi.org/10.1103/PHYSREVLETT.101.186801.

[85] S.S. Nkosi, P.S. Mkwae, S.A. Ogundipe, N. Leshabane, N. Revaprasadu, R.E. Kroon, Abnormal p-type to n-type switching during nitric oxide gas sensing: $Ni(OH)_2$ nanoplatelets on amorphous NiO seed layers, Vacuum 200 (2022) 111032, https://doi.org/10.1016/J.VACUUM.2022.111032.

[86] H.S. Kousar, D. Srivastava, A.J. Karttunen, M. Karppinen, G.C. Tewari, p-type to n-type conductivity transition in thermoelectric CoSbS, APL Mater. 10 (2022) 55, https://doi.org/10.1063/5.0107277/2835040.

[87] Y. Gong, X. Wu, X. Zhou, X. Li, N. Han, Y. Chen, High acetone sensitive and reversible P- to N-type switching NO_2 sensing properties of Pt@Ga-ZnO core-shell nanoparticles, Sens. Actuators B Chem. 289 (2019) 114–123, https://doi.org/10.1016/J.SNB.2019.03.085.

[88] A. Gurlo, N. Bârsan, A. Oprea, M. Sahm, T. Sahm, U. Weimar, An n- to p-type conductivity transition induced by oxygen adsorption on α-Fe_2O_3, Appl. Phys. Lett. 85 (2004) 2280–2282, https://doi.org/10.1063/1.1794853.

[89] Y. Liu, D. Zhao, W. Tang, T. Li, Q. You, G. Xie, Hydrothermal synthesis of monoclinic $CrVO_4$ nanoparticles and catalytic ammoxidation of 2-chlorotoluene, Catal. Lett. (2023) 1–8, https://doi.org/10.1007/S10562-023-04305-2.

[90] H. Ji, W. Zeng, Y. Li, Gas sensing mechanisms of metal oxide semiconductors: a focus review, Nanoscale 11 (2019) 22664–22684, https://doi.org/10.1039/C9NR07699A.

[91] V. Katari, S.J. Patwe, S.N. Achary, A.K. Tyagi, High temperature structural, dielectric, and ion conduction properties of orthorhombic $InVO_4$, J. Am. Ceram. Soc. 96 (2013) 166–173, https://doi.org/10.1111/J.1551-2916.2012.05447.X.

[92] V.D. Nithya, R. Kalai Selvan, Synthesis, electrical and dielectric properties of $FeVO_4$ nanoparticles, Phys. B Condens Matter 406 (2011) 24–29, https://doi.org/10.1016/J.PHYSB.2010.10.004.

[93] N. Barsan, U. Weimar, Conduction model of metal oxide gas sensors, J. Electroceram 7 (2001) 143–167, https://doi.org/10.1023/A:1014405811371.

[94] Z. Zhang, J.T. Yates, Band bending in semiconductors: chemical and physical consequences at surfaces and interfaces, Chem. Rev. 112 (2012) 5520–5551, https://doi.org/10.1021/cr3000626.

[95] M. Hübner, C.E. Simion, A. Tomescu-Stănoiu, S. Pokhrel, N. Bârsan, U. Weimar, Influence of humidity on CO sensing with p-type CuO thick film gas sensors, Sens Actuators B Chem. 153 (2011) 347–353, https://doi.org/10.1016/J.SNB.2010.10.046.

[96] J. Dhakshinamoorthy, B. Pullithadathil, New insights towards electron transport mechanism of highly efficient p-type CuO (111) nanocuboids-based H_2S gas sensor, J. Phys. Chem. C 120 (2016) 4087–4096, https://doi.org/10.1021/acs.jpcc.5b11327.

[97] J. Hu, D. Li, J.G. Lu, R. Wu, Effects on electronic properties of molecule adsorption on CuO surfaces and nanowires, J. Phys. Chem. C. 114 (2010) 17120–17126, https://doi.org/10.1021/jp1039089.

[98] B. Lyson-Sypien, M. Radecka, K. Świerczek, B. Lyson-Sypien, M. Radecka, M. Rekas, K. Swierczek, K. Michalow-Mauke, T. Graule, K. Zakrzewska, Grain-size-Dependent Gas-sensing Properties of TiO_2 Nanomaterials, 211, Elsevier, 2015, pp. 67–76, https://doi.org/10.1016/j.snb.2015.01.050.

[99] A. Reghu, L.J. Legore, J.F. Vetelino, R.J. Lad, B.G. Frederick, Distinguishing bulk conduction from band bending transduction mechanisms in chemiresistive metal oxide gas sensors, J. Phys. Chem. C 122 (2018) 10607–10620, https://doi.org/10.1021/acs.jpcc.8b01446.

David John Dmonte is currently pursuing his PhD in Nanotechnology and Advanced Materials. He is at the Centre of Polymer Systems, Tomas Bata University in Zlin, Czech Republic. His research interests include the synthesis, characterisation and performance evaluation of Semiconductor materials in thin films usage of Inkjet printing systems, focusing on their application in gas sensors.

Aman Bhardwaj An ardent materials scientist and electro-chemistry enthusiast. My present research focuses on developing novel materials and engineering strategies for energy conversion and storage devices. My skills and expertise includes- Materials synthesis (nanopowder, ceramic membranes, thin-films, and coatings) by chemical routes - Materials characterization, e.g., XRD, STEM, EDS, XPS, ICP-OES, AFM, BET, TG-DTA, Raman and IR, etc towards the Study of solid-fluid interfaces and structure-property relationships
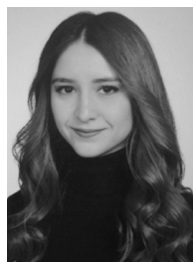
Pelin Kavraz received the MSc. degree in Solid State Physics from Istanbul University in 2023. Her research interests include inorganic nanomaterial design with electrospinning and its material characterization, with appropriate doping through chemical methodology for application focused on VOCs gas sensing.

Rostislav Slobodian is a PhD student at the Tomas Bata University in Zlin (TBU), Czech Republic at the Center of Polymer Systems. He received an MSc in Chemistry and Materials Technology from the Faculty of Technology, TBU Zlin. He is a junior researcher at the Systems with Sensoric Properties group at the Centre of Polymer Systems, TBU.

Jan Antos received the Ph.D. degree in Automatic Control and Informatics from Tomas Bata University in 2019. His research interests include predictive control, computer science, artificial intelligence, system identification, process control and measurement.

Orhan Sisman graduated from the 5-year integrated program in Physics Education with both B.Sc. and M.Sc. (without thesis) degrees at Middle East Technical University in 2013. He obtained another M.Sc. degree in Physics from Gebze Technical University in 2016. In 2020, he received his Ph.D. degree in Sensor Laboratory at the University of Brescia. Currently, he works as a postdoctoral researcher at the FunGlass Research Center, Alexander Dubcek University of Trencin, Slovakia. His research interests are sensor and energy applications of functional nanostructures, organic-inorganic hybrid materials, and MOX-based glass ceramics.

Sanjay Mathur Director of the Institute of Inorganic Chemistry at the University of Cologne, Germany is also the Director of the Institute of Renewable Energy Sources at the Xian Jiao Tong University, Xian, China and a World Class University Professor at the Chonbuk University in Korea. His research interests focus on nanomaterials and advanced ceramics for energy technologies. He holds 10 patents and has authored/co-authored > 425 original research publications and has edited several books.

Dusan Galusek professor of materials science, director of the Centre for Functional and Surface Functionalized Glass at the Alexander Dubcek University of Trencin, Slovakia. His research interests include transparent oxide ceramic materials with additional functionalities, aluminate glasses, corrosion of glass and ceramics, and materials for biomedial applications. He has authored/co-authored > 220 original research papers in peer reviewed journals, and several books.

Ivo Kuritka received the Ph.D. degree in Technology of macromolecular compounds from Tomas Bata University in Zlín (TBU) in 2005. He is an associate professor at the Faculty of Technology TBU since 2009 and a senior researcher at the Centre of Polymer Systems, TBU, since 2011. He is the author or co-author of 155 scientific articles in impacted journals indexed in WoS. His research interests include nanomaterials, synthesis of nanoparticles and preparation of nanocomposites, fabrication of devices and their spectroscopic characterisation.

Thomas Fischer Academic Councilor, Researcher and Project Manager at the University of Cologne. He holds several prestigious awards such as Global Young Investigator Award and Global Star Award etc. His research interest include metal-organic precursors, functionalized carbon nanotubes, Chemical Vapor Deposition (CVD) for various applications such as solar cells, gas sensing.etc.